

1
2 Supplementary Information for

3
4 **Structural basis for backtracking by the SARS-CoV-2 replication-**
5 **transcription complex**

6
7 **Brandon Malone^{1,8}, James Chen^{1,8}, Qi Wang², Eliza Llewellyn¹, Young Joo**
8 **Choi¹, Paul Dominic B. Olinares³, Xinyun Cao⁴, Carolina Hernandez⁵,**
9 **Edward T. Eng⁵, Brian T. Chait³, David E. Shaw^{2,6}, Robert Landick^{4,7},**
10 **Seth A. Darst^{1,9}, Elizabeth A. Campbell^{1,9,10}**

11 ¹Laboratory of Molecular Biophysics, The Rockefeller University, New York, NY,
12 10065 USA.

13 ²D. E. Shaw Research, New York, NY 10036 USA.

14 ³Laboratory of Mass Spectrometry and Gaseous Ion Chemistry, The Rockefeller
15 University, New York, NY, 10065 USA.

16 ⁴Department of Biochemistry, University of Wisconsin-Madison, Madison, WI
17 53706 USA.

18 ⁵The National Resource for Automated Molecular Microscopy, Simons Electron
19 Microscopy Center, New York Structural Biology Center, New York, NY, 10027
20 USA.

21 ⁶Department of Biochemistry and Molecular Biophysics, Columbia University,
22 New York, NY 10032 USA.

23 ⁷Department of Bacteriology, University of Wisconsin-Madison, Madison, WI
24 53706 USA.

25 ⁸These authors contributed equally: Brandon Malone, James Chen.

26 ⁹Correspondence to: darst@rockefeller.edu, campbee@rockefeller.edu

27
28

29 **Supplementary Information Text**

30

31 **METHODS**

32 Structural biology software was accessed through the SBGrid consortium (1).

33 **Protein expression and purification.**

34 *SARS-CoV-2 nsp12*. SARS-CoV-2 nsp12 was expressed and purified as
35 described (1). A pRSFDuet-1 plasmid expressing SARS-CoV-2 His₆-SUMO-
36 nsp12 (Addgene plasmid 159107) was transformed into *Escherichia coli* (*Eco*)
37 BL21-CodonPlus cells (Agilent). Cells were grown, followed by the addition of
38 isopropyl β-d-1-thiogalactopyranoside (IPTG) to induce protein expression
39 overnight. Cells were collected by centrifugation, resuspended and lysed in a
40 continuous-flow French press (Avestin). The lysate was cleared by centrifugation,
41 loaded onto a HiTrap Heparin HP column (Cytiva), and then eluted using a salt
42 gradient. The fractions containing nsp12 were pooled and loaded onto a HisTrap
43 HP column (Cytiva), washed, and eluted. Eluted nsp12 was dialyzed overnight in
44 the presence of His₆-Ulp1 SUMO protease. Cleaved nsp12 was passed through
45 a HisTrap HP column (Cytiva). Flow-through was collected, concentrated by
46 centrifugal filtration (Amicon), and loaded on a Superdex 200 HiLoad 16/600
47 (Cytiva) for size-exclusion chromatography. Glycerol was added to the purified
48 nsp12, aliquoted, flash frozen with liquid N₂, and stored at -80°C.

49 *SARS-CoV-2 nsp7/8*. SARS-CoV-2 nsp7/8 was expressed and purified as
50 described (1). The pCDFDuet-1 plasmid expressing SARS-CoV-2 His₆-ppx-
51 nsp7/8 (ppx is a Prescission Protease cleavage site; Addgene plasmid 159092)
52 was transformed into *Eco* BL21(DE3). Cells were grown and protein expression
53 was induced overnight by the addition of IPTG. Cells were collected by
54 centrifugation, resuspended, and lysed in a continuous-flow French press
55 (Avestin). The lysate was cleared by centrifugation, then loaded onto a HisTrap
56 HP column (Cytiva), washed, and eluted. Eluted nsp7/8 was dialyzed overnight in
57 the presence of His₆-Prescission Protease to cleave the His₆-tag. Cleaved nsp7/8
58 was passed through a HisTrap HP column (Cytiva). Flow-through was collected,

59 concentrated by centrifugal filtration (Amicon), and loaded onto a Superdex 75
60 Hiloal 16/600 (Cytiva). Glycerol was added to the purified nsp7/8, aliquoted,
61 flash frozen with liquid N₂, and stored at -80°C.

62 **SARS-CoV-2 nsp13.** SARS-CoV-2 nsp13 was expressed and purified as
63 described (1). The pet28 plasmid containing SARS-CoV-2 His₆-ppx-nsp13
64 (Addgene plasmid 159390) was transformed into *Eco* Rosetta(DE3) (Novagen).
65 Cells were grown, followed by the addition of IPTG to induce protein expression
66 overnight. Cells were collected by centrifugation, resuspended, and lysed in a
67 continuous-flow French press (Avestin). The lysate was cleared by centrifugation,
68 then loaded onto a HisTrap HP column (Cytiva), washed, and eluted. Eluted
69 nsp13 was dialyzed overnight in the presence of His₆-PreScission Protease to
70 cleave His₆-tag. Cleaved nsp13 was passed through a HisTrap HP column
71 (Cytiva). Flow-through was collected, concentrated by centrifugal filtration
72 (Amicon), and loaded onto a Superdex 200 Hiloal 16/600 (Cytiva). Glycerol was
73 added to the purified nsp13, aliquoted, flash frozen with liquid N₂, and stored at -
74 80°C.

75

76 **Native electrophoretic mobility shift assays.** Nsp12 or nsp12-D760A were
77 incubated with 3-fold molar excess of nsp7/8 in transcription buffer (120 mM K-
78 acetate, 20 mM HEPES pH 8, 10 mM MgCl₂, 2 mM DTT) to assemble holo-RdRp
79 (2 μM final). The resulting complex was incubated with 1 μM of annealed RNA
80 scaffold (Horizon Discovery) for 5 minutes at 30°C. Nsp13 and pre-mixed ADP
81 and AlF₃ (Sigma-Aldrich) were added to a final concentration of 2 μM and 2 mM,
82 respectively, and incubated for an additional 5 minutes at 30°C. Reactions were
83 analyzed by native gel electrophoresis on a 4.5% polyacrylamide native gel
84 (37.5:1 acrylamide:bis-acrylamide) in 1X TBE (89 mM Tris, 89 mM boric acid,
85 1 mM EDTA) at 4°C. The gel was stained with Gel-Red (Biotium).

86

87 **Native mass spectrometry (nMS) analysis.** The reconstituted sample
88 containing 4 μM RTC and 8 μM nsp13 incubated with 2 mM ADP-AlF₃ was

89 buffer-exchanged into 150 mM ammonium acetate, 0.01% Tween-20, pH 7.5
90 using a Zeba microspin desalting column with a 40 kDa MWCO (ThermoFisher
91 Scientific). For nMS analysis, a 2–3 μL aliquot of the buffer-exchanged sample
92 was loaded into a gold-coated quartz capillary tip that was prepared in-house and
93 then electrosprayed into an Exactive Plus with extended mass range (EMR)
94 instrument (Thermo Fisher Scientific) with a static direct infusion nanospray
95 source (2). The MS parameters used: spray voltage, 1.2 kV; capillary
96 temperature, 150 $^{\circ}\text{C}$; in-source dissociation, 0 V; S-lens RF level, 200; resolving
97 power, 17,500 at m/z of 200; AGC target, 1×10^6 ; maximum injection time,
98 200 ms; number of microscans, 5; injection flatapole, 6 V; interflatapole, 4 V; bent
99 flatapole, 4 V; high energy collision dissociation (HCD), 200 V; ultrahigh vacuum
100 pressure, 7.2×10^{-10} mbar; total number of scans, at least 100. Mass calibration
101 in positive EMR mode was performed using cesium iodide. For data processing,
102 the acquired MS spectra were visualized using Thermo Xcalibur Qual Browser
103 (v. 4.2.47). MS spectra deconvolution was performed either manually or using
104 the software UniDec v. 4.2.0 (3, 4). The following parameters were used for the
105 UniDec processing: m/z range, 7,000 – 10,000 Th; background subtraction,
106 subtract curved at 100; smooth charge state distribution, enabled; peak shape
107 function, Gaussian; Beta Softmax distribution parameter, 20.

108 The expected masses for the component proteins based on previous nMS
109 experiments (1) include nsp7: 9,137 Da; nsp8 (N-terminal Met lost): 21,881 Da;
110 nsp13 (post-protease cleavage, has three Zn^{2+} ions coordinated with
111 9 deprotonated cysteine residues): 67,464 Da, and nsp12 (has two Zn^{2+} ions
112 coordinated with 6 deprotonated cysteine residues): 106,785 Da. The mass of
113 the assembled RNA duplex scaffold is 30,512 Da.

114 Experimental masses were reported as the average mass \pm standard
115 deviation (S.D.) across all the calculated mass values within the observed charge
116 state series. Mass accuracies were calculated as the % difference between the
117 measured and expected masses relative to the expected mass. The observed
118 mass accuracies ranged from 0.016 – 0.035%.

119 **Preparation of SARS-CoV-2 nsp13-BTC₅ for Cryo-EM.** Purified nsp12 and
120 nsp7/8 were mixed in a 1:3 molar ratio and incubated at 22° C for 15 minutes.
121 The mixture was buffer-exchanged into cryo-EM buffer (20 mM HEPES pH 8.0,
122 150 mM K-acetate, 10 mM MgCl₂, 1 mM DTT) using Zeba desalting columns
123 (ThermoFisher Scientific) and incubated with annealed BTC₅-scaffold (Fig. 1A) in
124 a 1:1.5 molar ratio. Purified nsp13 was concentrated by centrifugal filtration
125 (Amicon) and buffer exchanged into cryo-EM buffer using Zeba desalting
126 columns. Buffer exchanged nsp13 was mixed with ADP and AlF₃ and then added
127 to nsp7/8/12/RNA scaffold at a molar ratio of 1:1 with a final concentration of
128 2 mM ADP-AlF₃. Complex was incubated for 5 minutes at 30° C and further
129 concentrated by centrifugal filtration (Amicon).

130

131 **Cryo-EM grid preparation.** Prior to grid freezing, 3-([3-
132 cholamidopropyl]dimethylammonio)-2-hydroxy-1-propanesulfonate (CHAPSO,
133 Anatrace) was added to the sample (8 mM final), resulting in a final complex
134 concentration of 10 μM. The final buffer condition for the cryo-EM sample was
135 20 mM HEPES pH 8.0, 150 mM K-acetate, 10 mM MgCl₂, 1 mM DTT,
136 2 mM ADP-AlF₃, 8 mM CHAPSO. C-flat holey carbon grids (CF-1.2/1.3-4Au,
137 Electron Microscopy Sciences) were glow-discharged for 20 s prior to the
138 application of 3.5 μL of sample. Using a Vitrobot Mark IV (ThermoFisher
139 Scientific), grids were blotted and plunge-frozen into liquid ethane with 90%
140 chamber humidity at 4°C.

141

142 **Cryo-EM data acquisition and processing.** Structural biology software was
143 accessed through the SBGrid consortium (5). Grids were imaged using a 300 kV
144 Titan Krios (ThermoFisher Scientific) equipped with a K3 camera (Gatan) and a
145 BioQuantum imaging filter (Gatan). Images were recorded using Legikon (6) with
146 a pixel size of 1.065 Å/px (micrograph dimensions of 5,760 x 4,092 px) over a
147 nominal defocus range of -0.8 μm to -2.5 μm and 30 eV slit width. Movies were
148 recorded in "counting mode" (native K3 camera binning 2) with ~30 e-/px/s in

149 dose-fractionation mode with subframes of 50 ms over a 2.5 s exposure (50
150 frames) to give a total dose of ~ 66 e-/Å. Dose-fractionated movies were gain-
151 normalized, drift-corrected, summed, and dose-weighted using MotionCor2 (7).
152 The contrast transfer function (CTF) was estimated for each summed image
153 using the Patch CTF module in cryoSPARC v2.15.0 (8) Particles were picked
154 and extracted from the dose-weighted images with box size of 256 px using
155 cryoSPARC Blob Picker and Particle Extraction. The entire dataset consisted of
156 10,685 motion-corrected images with 4,961,691 particles. Particles were sorted
157 using cryoSPARC 2D classification (N=100), resulting in 2,412,034 curated
158 particles. Initial models (Ref 1: decoy 1, Ref 2: complex, Ref 3: decoy 2;
159 SI Appendix; Fig. S2) were generated using cryoSPARC *ab initio* Reconstruction
160 on a subset of 85,398 particles. Particles were further curated using Ref 1-3 as
161 3D templates for cryoSPARC Heterogeneous Refinement (N=6), resulting in the
162 following: class1 (Ref 1), 258,097 particles; class2 (Ref 1), 263,966 particles;
163 class3 (Ref 2), 668,743 particles; class4 (Ref 2), 665,480 particles; class5 (Ref
164 3), 280,933 particles; class6 (Ref 3), 274,815 particles. Particles from class3 and
165 class4 were combined and further curated with another round of Heterogeneous
166 Refinement (N=6), resulting in the following: class1 (Ref 1), 67,639 particles;
167 class2 (Ref 1), 61,097 particles; class3 (Ref 2), 553,368 particles; class4 (Ref 2),
168 554,581 particles; class5 (Ref 3), 42,114 particles; class6 (Ref 3), 55,424
169 particles. Curated particles from class3 and class4 were combined, re-extracted
170 with a box size of 320 px, and further classified using Ref 2 as a 3D template for
171 cryoSPARC Heterogeneous Refinement (N=4). Classes from this round of
172 Heterogeneous Refinement (N=4) were as follows: class1 (Ref 2), 871,163
173 particles; class2 (Ref 2), 77,769 particles; class3 (Ref 2), 61,489 particles; class4
174 (Ref 2), 64,026 particles. Particles from class1 and class2 were combined and
175 further sorted using Heterogeneous Refinement (N=4) using class maps as
176 templates, resulting in the following: class1, 134,536 particles; class2, 270,170
177 particles; class3, 294,162 particles; class4, 172,295 particles. Classification
178 revealed two unique classes: nsp13₁-BTC (class1 and class2) and nsp13₂-BTC
179 (class3 and class4). Particles within each class were further processed using

180 RELION 3.1-beta Bayesian Polishing(9, 10). Polished particles were refined
181 using cryoSPARC Non-uniform Refinement, resulting in structures with the
182 following particle counts and nominal resolutions: nsp13₁-BTC (404,706 particles;
183 3.40 Å) and nsp13₂-BTC (466,457 particles; 3.45 Å).

184 To improve the resolution of the RNA in the BTC, particles from both
185 classes were combined in a cryoSPARC Non-uniform Refinement and density
186 corresponding to nsp13 was subtracted. Subtracted particles were further refined
187 with cryoSPARC Local Refinement using a mask encompassing the BTC and a
188 fulcrum point defined on the backtracked RNA. This map, BTC₅(local), contained
189 871,163 particles with a nominal resolution of 3.23 Å.

190 To improve the density of nsp13.2 in the nsp13₂-BTC map, particles were
191 subtracted using a mask defined around nsp13.2, leaving residual signal for only
192 nsp13.2. Subtracted particles were classified (N=4) in RELION 3.1 beta using a
193 mask around nsp13.2, resulting in the following classes: class1, 71,607 particles;
194 class2, 163,540 particles; class3, 176,461 particles; class4, 54,849 particles.
195 Subtracted particles in class1 and class2 were combined and reverted back to
196 the original particles, followed by refinement using cryoSPARC Non-uniform
197 Refinement. The resulting map of nsp13₂-BTC contains 235,147 particles with
198 nominal resolution of 3.59 Å. Local resolution calculations were generated using
199 blocres and blocfilt from the Bsoft package (11).

200

201 **Model building and refinement.** Initial models were derived from PDB: 6XEZ
202 (1). The models were manually fit into the cryo-EM density maps using Chimera
203 (12) and rigid-body and real-space refined using Phenix real_space_refine (13).
204 For real-space refinement, rigid body refinement was followed by all-atom and B-
205 factor refinement with Ramachandran and secondary structure restraints. Models
206 were inspected and modified in Coot (14).

207

208 **4-thiouridine crosslinking.** Nsp12 or nsp12-D760A were incubated with 3-fold
209 molar excess of nsp7/8 to assemble holo-RdRp (2 μ M final) in transcription
210 buffer. The resulting holo-RdRp was added to a modified RNA scaffold
211 (SI Appendix; Fig. S5A) containing a photoactivable 4-thiouridine base (Horizon
212 Discovery) which was 5'-labelled by T4-polynucleotide kinase (New England
213 Biolabs) with γ -³²P-ATP (Perkin-Elmer). The holo-RdRp/RNA complex was left to
214 incubate for 5 minutes at 30°C in the dark. Nsp13 and ATP were added to a final
215 concentration of 2 μ M and 2 mM, respectively, and incubated for five minutes at
216 30°C in the dark. The reaction mixture was transferred to a Parafilm covered
217 aluminum block at 4°C and irradiated with a 365-nm handheld UV lamp.
218 Reactions were quenched with LDS sample loading buffer (ThermoFisher
219 Scientific) and analyzed by gel electrophoresis on a NuPAGE 4-12% Bis-Tris gel
220 (ThermoFisher) at 150 Volts for 1 hour and visualized by autoradiography.

221

222 **Molecular dynamics simulations**

223 *General simulation setup and parameterization.* Proteins, ADP, and ions were
224 parameterized with the DES-Amber SF1.0 force field (15). RNAs were
225 parameterized with the Amber ff14 RNA force field (16) with modified
226 electrostatic, van der Waals, and torsional parameters to more accurately
227 reproduce the energetics of nucleobase stacking (17). The systems were
228 solvated with water parameterized with the TIP4P-D water model (18) and
229 neutralized with 150 mM NaCl buffer. The systems each contained ~887,000
230 atoms in a 190 \times 190 \times 190 Å cubic box.

231 Systems were first equilibrated on GPU Desmond using a mixed
232 NVT/NPT schedule (19), followed by a 1 μ s relaxation simulation on Anton, a
233 special-purpose machine for molecular dynamics simulations (20). All production
234 simulations were performed on Anton and initiated from the last frame of the
235 relaxation simulation. Production simulations were performed in the NPT
236 ensemble at 310 K using the Martyna-Tobias-Klein barostat (21). The simulation
237 time step was 2.5 fs, and a modified r-RESPA integrator (22, 23) was used in

238 which long-range electrostatic interactions were evaluated every three time
239 steps. Electrostatic forces were calculated using the *u*-series method (24). A 9-Å
240 cutoff was applied for the van der Waals calculations.

241 *System preparation.* The nsp13₂-BTC_{-1U+1C} and the nsp13₂-BTC_{-1U+1U} complexes
242 were prepared from the cryo-EM structure of the nsp13₂-BTC₅. AlF₃ and
243 CHAPSO were removed. Cytosines at the +2 and +3 positions of the p-RNA
244 were removed, and the cytosine at -1 was mutated to uracil. The resulting p-
245 RNA had a matched -1U and a mismatched +1C in nsp13₂-BTC_{-1U+1C}, and a
246 matched -1U and +1U in nsp13₂-BTC_{-1U+1U}. Missing loops and termini in
247 proteins were capped with ACE/NME capping groups. Missing RNA nucleotides
248 (chain T +7 to +3) were manually added. The two complexes were prepared for
249 simulation using the Protein Preparation Wizard in Schrödinger Maestro. After a
250 1 μs relaxation simulation of the nsp13₂-BTC_{-1U+1C} complex, the -1U of the p-
251 RNA formed a Watson-Crick base pair with the -1A in the t-RNA, and the +1C of
252 p-RNA formed a non-Watson-Crick C-A hydrogen bond with the +1A of the t-
253 RNA in the active site. After a 1 μs relaxation simulation of the nsp13₂-BTC_{-1U+1U}
254 complex, the -1U and +1U of the p-RNA formed Watson-Crick base pairs with
255 the -1A and +1A of the t-RNA respectively.

256 *Simulation analysis.* All simulations were visually inspected using the in-house
257 visualization software Firefly. The average root-mean-square deviation (RMSD)
258 was calculated for +1C (or +1U) of the p-RNA between the last frame of the 1 μs
259 relaxation simulation and instantaneous structures from the trajectories, aligned
260 on the entire nps12 module.

261

262 **Quantification and statistical analysis.** The nMS spectra were visualized using
263 Thermo Xcalibur Qual Browser (versions 3.0.63 and 4.2.27), deconvolved using
264 UniDec versions 3.2 and 4.1 (3, 4) and plotted using the m/z software
265 (Proteometrics LLC, New York, NY). Experimental masses (SI Appendix;
266 Fig. S1B and C) were reported as the average mass ± standard deviation across

267 all the calculated mass values obtained within the observed charge state
268 distribution.

269 The local resolution of the cryo-EM maps (SI Appendix; Fig. S3B-D) was
270 estimated using blocres (11) with the following parameters: box size 15, sampling
271 1.1, and cutoff 0.5. Directional 3D FSC (SI Appendix; Fig. S3H-J) were calculated
272 by 3DFSC (25). The quantification and statistical analyses for model refinement
273 and validation were generated using MolProbity (26) and PHENIX (13).

274

275

276

277

278

279

280

281

282

283

284

285

286

287

288

289

290

291

292

293 **Table S1. Cryo-EM data collection, refinement, and validation statistics.**

294

	nsp7/8/12/13/BTC_scaffold/ADP-AIF₃/CHAPSO		
Sample ID	nsp13 ₁ -BTC	nsp13 ₂ -BTC	BTC (local)
EMDB	EMD-23007	EMD-23008	EMD-23009
PDB	7KRN	7KRO	7KRP
Data collection and processing			
Microscope		TFS Titan Krios	
Voltage (kV)		300	
Detector		Gatan K3 Camera	
Electron exposure (e ⁻ /Å ²)		66	
Defocus range (µm)		-0.8 to -2.5	
Data collection mode		Counting Mode	
Nominal Magnification		81,000x	
Pixel size (Å)		1.065	
Symmetry imposed		C1	
Initial particle images (no.)		4,961,691	
Final particle images (no.)	404,706	235,147	871,163
Map resolution (Å) - FSC threshold 0.143	3.40	3.59	3.23
Map resolution range (Å)	2.5-5.0	2.5-5.0	2.5-5.1
Refinement			
Initial model used (PDB code)	6XEZ	6XEZ	6XEZ
Map sharpening B factor (Å ²)	-139.6	-127.6	-103.9

Model composition			
Non-hydrogen atoms	17351	21988	12561
Protein residues	1963	2553	1373
Nucleic acid residues	80	80	73
Ligands	5 Zn ²⁺ , 2 Mg ²⁺ , 3 CHAPSO, 2 ADP, 1 AlF ₃	8 Zn ²⁺ , 3 Mg ²⁺ , 3 CHAPSO, 3 ADP, 2 AlF ₃	2 Zn ²⁺ , 1 Mg ²⁺ , 3 CHAPSO, 1 ADP
B factors (Å ²)			
Protein	45.65	74.56	38.31
Nucleic acid	128.79	163.6	140.77
Ligands	59.03	78.99	46.55
R.m.s. deviations			
Bond lengths (Å)	0.007	0.007	0.004
Bond angles (°)	0.711	0.735	0.609
Validation			
MolProbity score	2.66	2.68	1.97
Clashscore	9.18	8.96	6.12
Poor rotamers (%)	7.54	9.4	4.18
Ramachandran plot			
Favored (%)	91.4	92.76	97.07
Allowed (%)	8.6	6.93	2.93
Disallowed (%)	0	0.31	0

295

296

297

298

Table S2. Comparison of nsp13₁-BTC₅ and nsp13₂-BTC₅ structures.

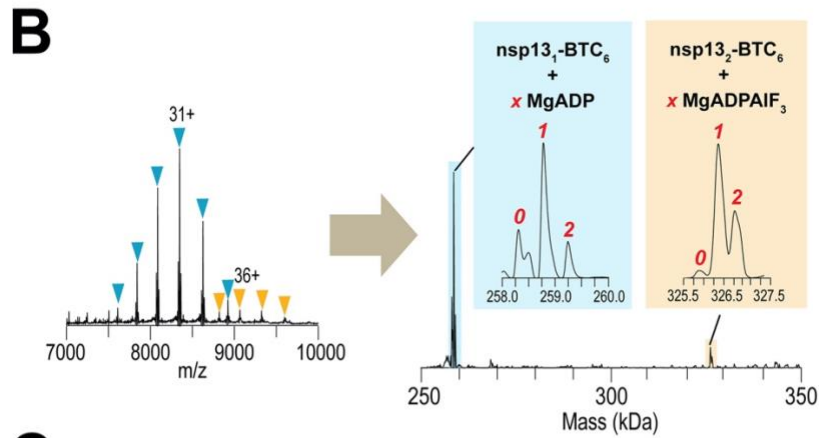
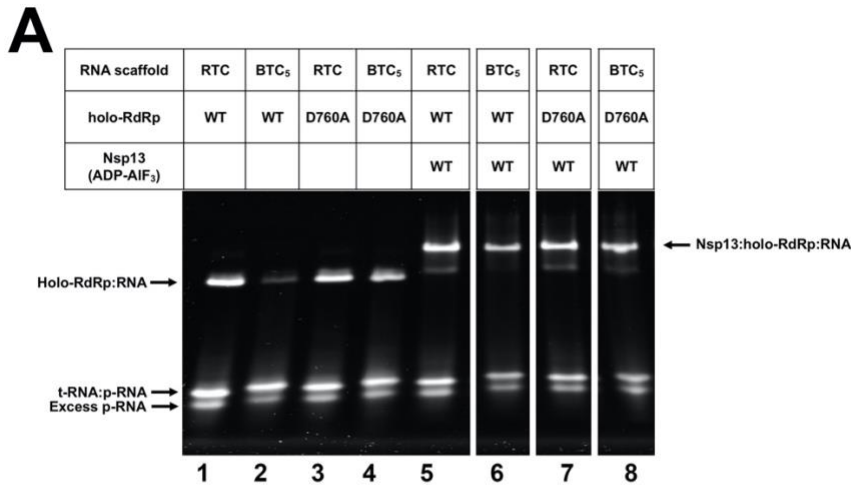
	PyMOL align command over all α -carbons ^a	PyMOL align command over nsp12 α -carbons ^b	
root-mean-square deviation (Å) (# of α -carbons included in alignment)	0.459 (1336)	0.214 (853)	
subunit	rms_cur	rms_cur	
nsp12	0.298 (927)	0.278 (927)	
nsp8a	1.288 (186)	1.411 (186)	N-term ext. (residues 1-98): 1.965 residues 99-186: 0.345
nsp7	0.333 (75)	0.337 (75)	
nsp8b	0.841 (185)	0.912 (185)	N-term ext. (residues 1-82): 1.116 residues 83-186: 0.737
nsp13.1	8.378 (590)	8.332 (590)	

299

300 ^aPyMOL command: align (nsp13₁-BTC₅ and name CA),(nsp13₂-BTC₅ and name CA)301 ^bPyMOL command: align (nsp13₁-BTC₅ and chain A and name CA),(nsp13₂-BTC₅

302 and chain A and name CA)

303 **SUPPLEMENTAL FIGURES**



C

Mass assignments from nMS analysis of BTC₆ incubated with nsp13 and MgADPAIF₃

Protein Assembly	Measured Mass ± SD (Da) [*]	Expected Mass (Da)	Δ Mass (Da)	% Mass Error
nsp13 ₁ -BTC ₆	258,307 ± 2	258,264	42	0.02
nsp13 ₁ -BTC ₆ + 1 MgADP	258,782 ± 3	258,716	66	0.03
nsp13 ₁ -BTC ₆ + 2 MgADP	259,246 ± 4	259,167	78	0.03
nsp13 ₂ -BTC ₆	325,844 ± 34	325,729	116	0.04
nsp13 ₂ -BTC ₆ + 1 MgADPAIF ₃	326,342 ± 18	326,264	78	0.02
nsp13 ₂ -BTC ₆ + 2 MgADPAIF ₃	326,776 ± 17	326,716	60	0.02

^{*} Calculated from the average and S.D. of all the measured masses across the charge-state distribution ($n \geq 4$).

304

305 **Fig. S1. Native gel electrophoresis mobility shift assay and nMS analysis of**
 306 **the BTC.**

307 **A.** A native gel electrophoretic mobility shift assay reveals that wt-holo-RdRp
308 requires nsp13(ADP-AIF₃) to bind the BTC₅-scaffold efficiently (compare lanes 1,
309 2, and 6) but holo-RdRp with nsp12-D760A does not require nsp13 (lane 4).

310 **B.** The nMS spectrum and the deconvolved mass spectrum showing assembly of
311 stable nsp13-BTC₆, formed on a scaffold identical to the BTC₅-scaffold except
312 with six mismatched C's at the p-RNA 3'-end. The peak for the nsp13₂-BTC₆
313 assembly is present at about ~9% intensity relative to the predominant peak from
314 nsp13₁-BTC₆. While most of the biochemical and structural analyses were done
315 using the BTC₅-scaffold, we do not expect major differences in the behavior of
316 BTC₆ compared to BTC₅.

317 **C.** Mass assignments of the deconvolved peaks from the nMS analysis.

318

319

320

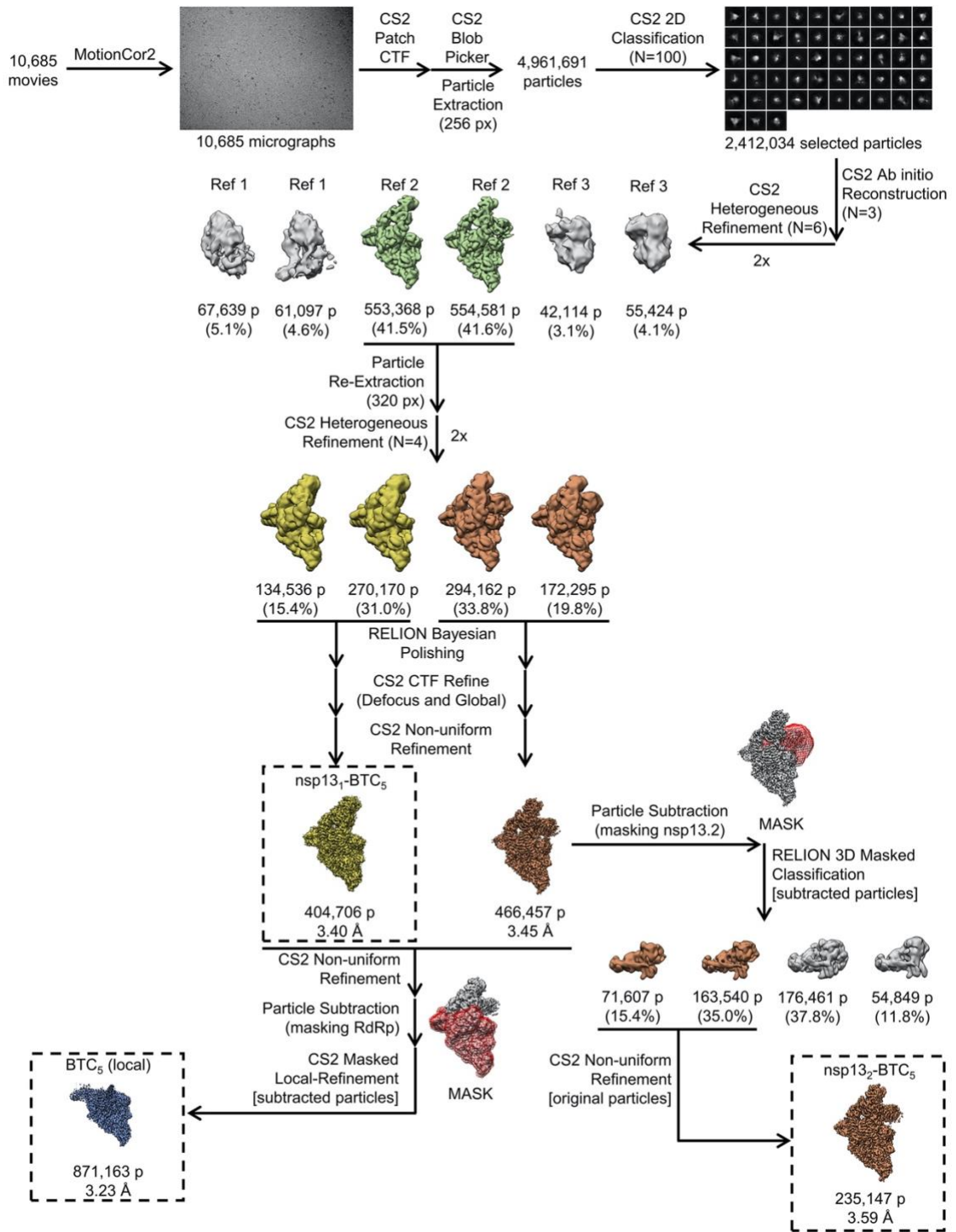
321

322

323

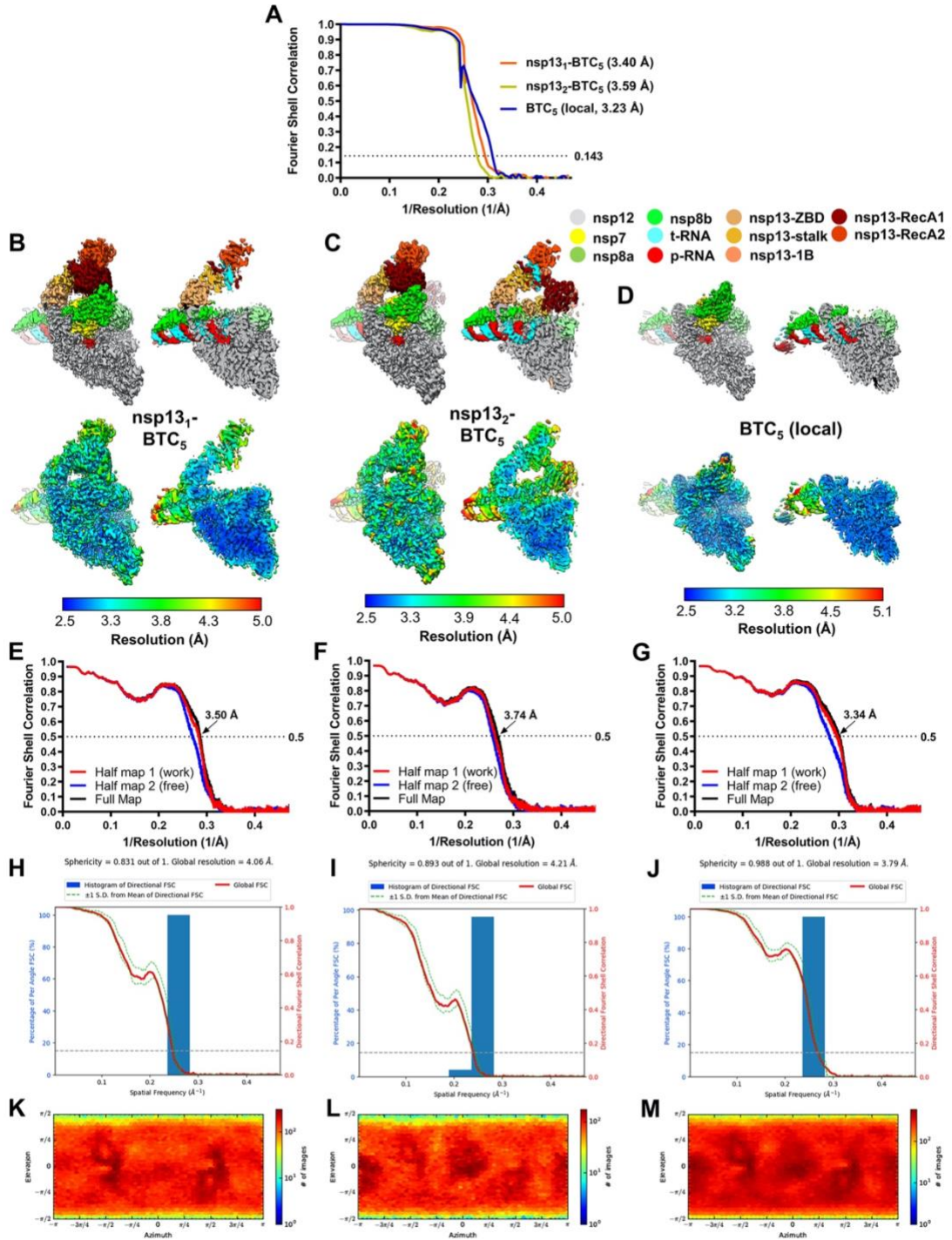
324

325



326

327 **Fig. S2. Cryo-EM processing pipeline.**



328

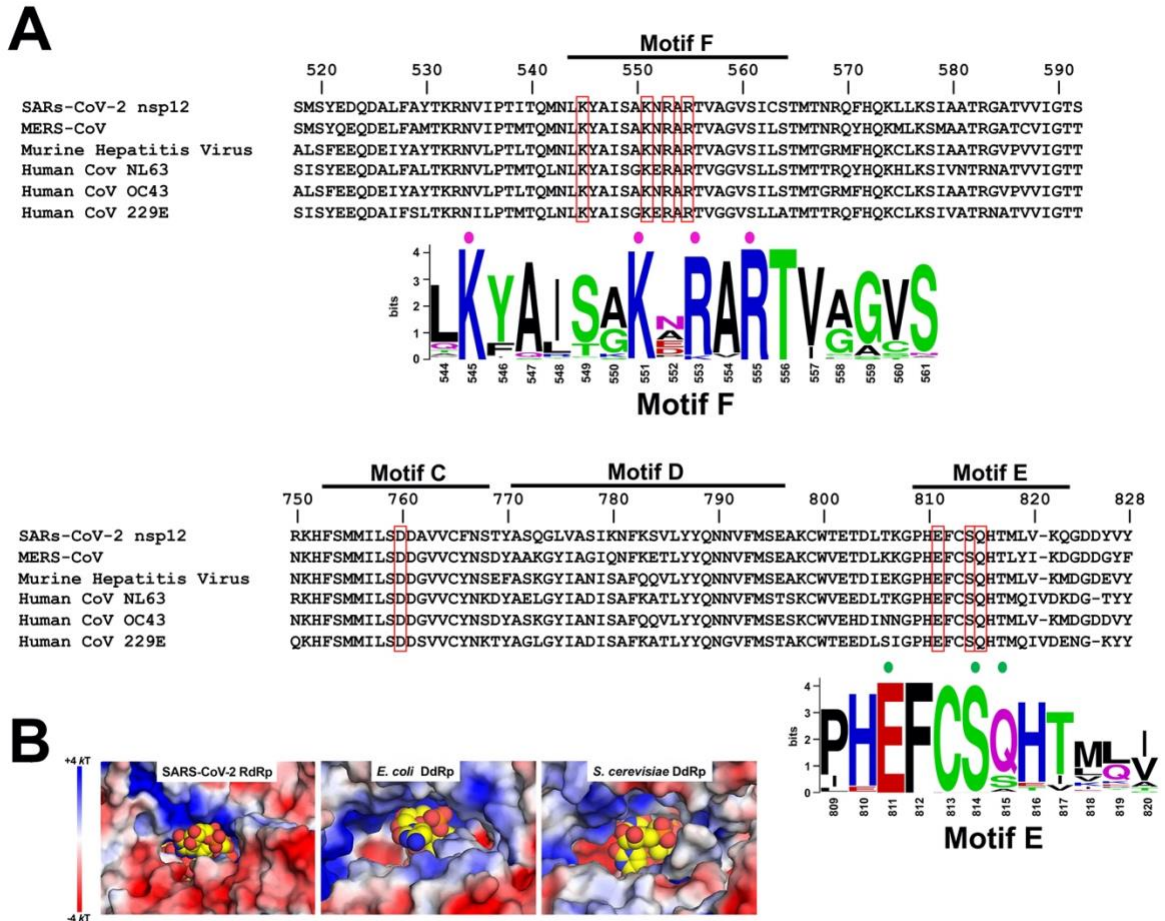
329

Fig. S3. Cryo-EM analysis.

330

A. Gold-standard FSC plots for nsp13₁-BTC₅, nsp13₂-BTC₅, and BTC₅(local),
331 calculated by comparing two independently determined half-maps from
332 cryoSPARC (8). The dotted line represents the 0.143 FSC cutoff.

333 **B-D.** Cryo-EM reconstructions filtered by local resolution(11). The view on the
334 right is a cross-section.
335 *(top)* Colored by subunit according to the color key.
336 *(bottom)* Color by local resolution (key on the bottom).
337 **B.** Nsp13₁-BTC₅.
338 **C.** Nsp13₂-BTC₅.
339 **D.** BTC₅(local).
340 **E – G.** FSC calculated between the refined structures and the half map used for
341 refinement (work, red), the other half map (free, blue), and the full map (black).
342 **E.** Nsp13₁-BTC₅.
343 **F.** Nsp13₂-BTC₅.
344 **G.** BTC₅(local).
345 **H - J,** Directional 3D Fourier shell correlation plots, calculated by 3DFSC(25).
346 **H.** Nsp13₁-BTC₅.
347 **I.** Nsp13₂-BTC₅.
348 **J.** BTC₅(local).
349 **K – M.** Particle angular distribution plots calculated in cryoSPARC. Scale shows
350 the number of particles assigned to a particular angular bin. Blue, a low number
351 of particles; red, a high number of particles.
352 **K.** Nsp13₁-BTC₅.
353 **L.** Nsp13₂-BTC₅.
354 **M.** BTC₅(local).
355
356
357
358



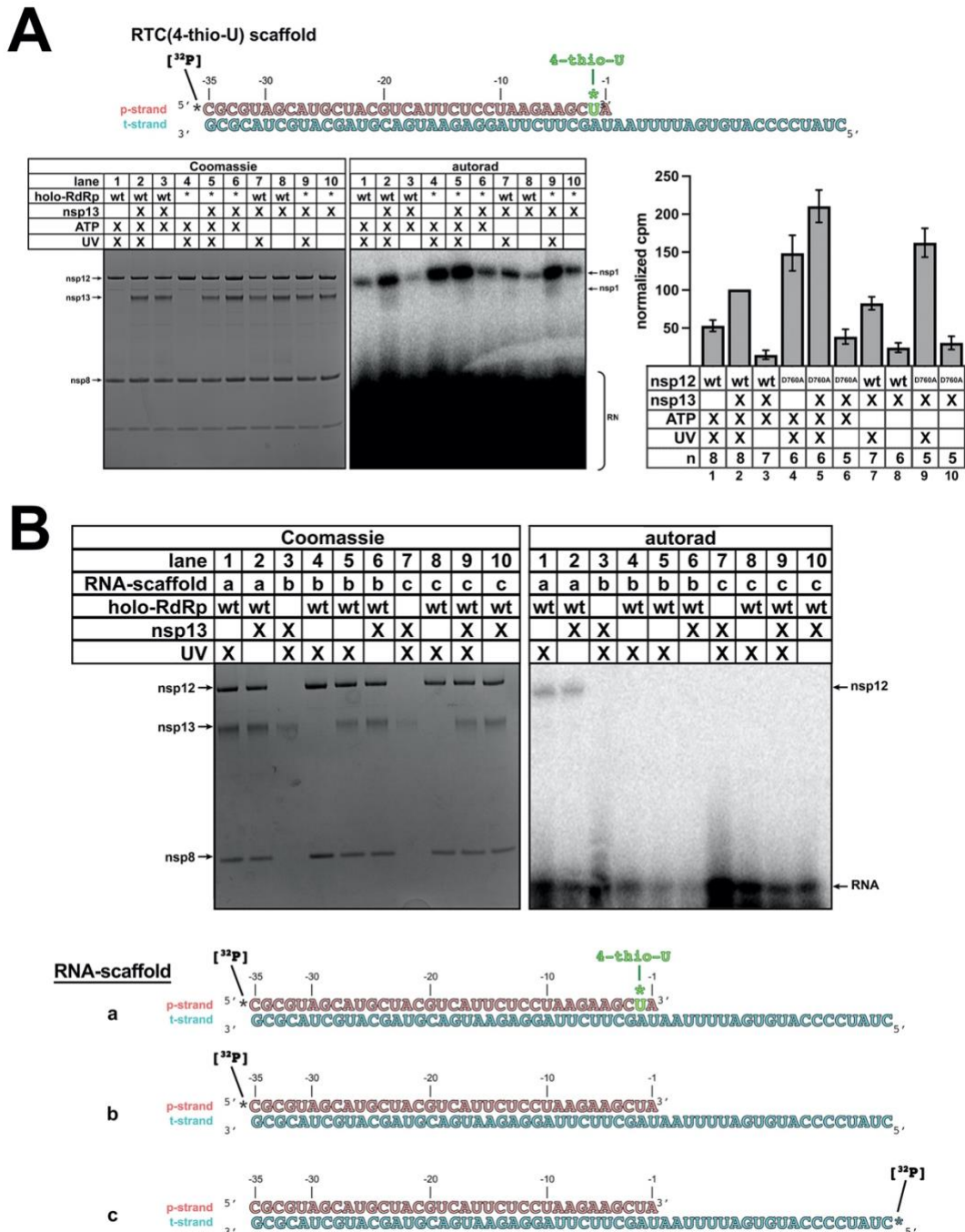
359

360 **Fig. S4. Sequence conservation of nsp12 homologs and NTP-entry tunnel**
 361 **environment.**

362 **A.** Sequence alignment of nsp12 homologs from six pathogenic and model CoV
 363 family members, covering RdRp motifs (27) (motifs F, C, D, and E denoted at the
 364 top of the sequence alignment) architecturally important for the NTP-entry tunnel.
 365 Selected residues discussed in the text are highlighted (red outlines). Sequence
 366 logos(28) for motif F and motif E are shown, with residues that interact with the
 367 backtracked RNA highlighted (colored dots above; see Figure 4). The sequence
 368 logos were generated from an alignment of 97 RdRp sequences from α -, β -, γ -,
 369 and δ -CoVs (Data S1).

370 **B.** Views from the outside into the NTP-entry tunnels of the SARS-CoV-2 BTC
 371 (left), an *E. coli* DdRp BTC [PDB ID: 6RI9; (29)] and an *S. cerevisiae* DdRp BTC
 372 [PDB ID: 3GTP; (30)]. Protein surfaces are colored by the electrostatic surface

373 potential [calculated using APBS; (31)]. Backtracked RNA is shown as atomic
374 spheres with yellow carbon atoms.
375



376

377

Fig. S5. 4-thio-U crosslinking analysis.

378

A. Protein-RNA crosslinking analysis: The 5'-[32P]-labelled RTC(4-thio-U)-scaffold

379

and the indicated proteins were incubated along with 2 mM ATP (when present),

380

exposed to UV as indicated, then analyzed by SDS polyacrylamide gel

381

electrophoresis and autoradiography. The positions of nsp8, nsp12, and nsp13

382

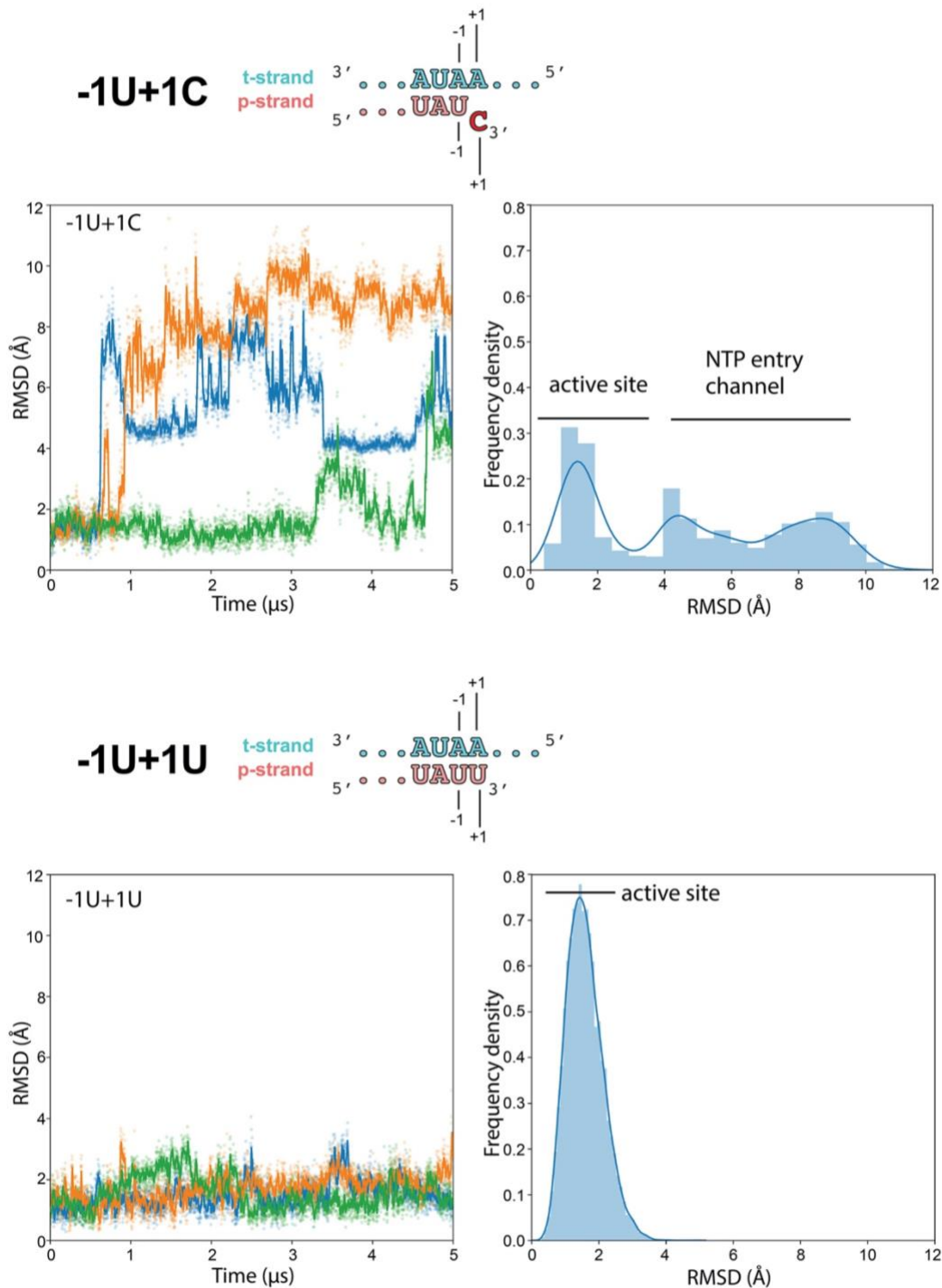
bands are indicated. Holo-RdRp(*) denotes the nsp12-D760A substitution that

383 facilitates backtracking (see Figure S1A). The two panels show the same SDS
384 polyacrylamide gel (left gel, Coomassie stained; right gel, visualized by
385 autoradiography). The histogram at the far right shows the results of quantitation
386 of the band corresponding to nsp12 by phosphorimager using ImageJ (32). The
387 error bars denote standard error of the mean (SEM) based on the number of
388 replicates denoted by 'n'. The results between experiments were normalized by
389 equalizing the counts of lane 2 (hence no error bar is shown).

390 **B.** Protein-RNA crosslinks are specific. Lanes 1, 2; Analysis using the 5'-[³²P]-
391 RTC(4-thio-U)-scaffold (RNA-scaffold 'a' shown on the bottom). Crosslinking to
392 nsp12 serves as a positive control for the crosslinking reaction. Lanes 3-6;
393 Analysis using RNA-scaffold 'b' (RTC-scaffold with 5'-[³²P]-labelled p-RNA).
394 Lanes 7-10: Analysis using RNA-scaffold 'c' (RTC-scaffold with 5'-[³²P]-labelled t-
395 RNA). The complete absence of protein-RNA crosslinks in lanes 3-10 indicates
396 that the observed protein-RNA crosslinks arise from the 4-thio-U site-specifically
397 incorporated in the p-RNA of the RTC(4-thio-U)-scaffold.

398

399



400

401 **Fig. S6. Molecular dynamics simulations of nsp13₂-BTC_{1U+1C} vs.**

402 **nsp13₂-BTC_{-1U+1U}.**

403 Molecular dynamics simulations of the nsp13₂-BTC_{-1U+1C} (*top*) and nsp13₂-BTC-

404 _{1U+1U} (*bottom*) complexes. The complexes were simulated with 3 replicates

405 (green, blue, and orange traces). The schematics illustrate the active-site

406 proximal nucleotides in each modeled complex. Each complex was simulated
407 with 3 replicates. RMSD values plotted as a function of time represent the heavy-
408 atom RMSD of the +1 nucleotide of the p-RNA (+1C for nsp13₂-BTC-_{1U+1C} or
409 matched +1U for nsp13₂-BTC-_{1U+1U}) compared with the starting configuration
410 (see Methods). The RMSD histograms (plotted on the right) are aggregates of all
411 3 replicates.

412 (*top*) Nsp13₂-BTC-_{1U+1C}. As shown in Figure 5C, the mismatched p-RNA +1C
413 spends about 60% of the time frayed from the t-RNA +1A and near or in the
414 NTP-entry tunnel (RMSD $\geq \sim 3.5$ Å).

415 (*bottom*) Nsp13₂-BTC-_{1U+1U}. With the p-RNA +1U matched with the t-RNA +1A for
416 Watson-Crick base pairing, the p-RNA +1U does not fray and spends all of its
417 time in the vicinity of the RdRp active site and base paired with the t-RNA.

418

419

420

421

422

423

424

425

426

427

428

429 **SUPPLEMENTAL DATA FILES**

430

431 **Data File S1.** Sequence alignment (Clustal format) of α - and β -CoV nsp12

432 sequences.

433

434 **SI References**

435

436 1. J. Chen, *et al.*, Structural basis for helicase-polymerase coupling in the SARS-
437 CoV-2 replication-transcription complex. *Cell* **182**, 1560-1573.e13 (2020).

438 2. P. D. B. Olinares, B. T. Chait, Methods in Molecular Biology. *Methods Mol*
439 *Biology Clifton N J* **2062**, 357–382 (2019).

440 3. D. J. Reid, *et al.*, High-Throughput Deconvolution of Native Mass Spectra. *J*
441 *Am Soc Mass Spectrom* **30**, 118–127 (2019).

442 4. M. T. Marty, *et al.*, Bayesian deconvolution of mass and ion mobility spectra:
443 from binary interactions to polydisperse ensembles. *Analytical chemistry* **87**,
444 4370–4376 (2015).

445 5. A. Morin, *et al.*, Collaboration gets the most out of software. *eLife* **2**, e01456
446 (2013).

447 6. C. Suloway, *et al.*, Automated molecular microscopy: the new Legimon system.
448 *Journal of structural biology* **151**, 41–60 (2005).

449 7. S. Q. Zheng, *et al.*, MotionCor2: anisotropic correction of beam-induced
450 motion for improved cryo-electron microscopy. *Nature methods* **14**, 331–332
451 (2017).

452 8. A. Punjani, J. L. Rubinstein, D. J. Fleet, M. A. Brubaker, cryoSPARC:
453 algorithms for rapid unsupervised cryo-EM structure determination. *Nat Methods*
454 **14**, 290–296 (2017).

455 9. S. H. W. Scheres, RELION: implementation of a Bayesian approach to cryo-
456 EM structure determination. *Journal of structural biology* **180**, 519–530 (2012).

- 457 10. J. Zivanov, *et al.*, New tools for automated high-resolution cryo-EM structure
458 determination in RELION-3. *eLife* **7** (2018).
- 459 11. G. Cardone, J. B. Heymann, A. C. Steven, One number does not fit all:
460 mapping local variations in resolution in cryo-EM reconstructions. *Journal of*
461 *structural biology* **184**, 226–236 (2013).
- 462 12. E. F. Pettersen, *et al.*, UCSF Chimera--a visualization system for exploratory
463 research and analysis. *Journal of computational chemistry* **25**, 1605–1612
464 (2004).
- 465 13. P. D. Adams, *et al.*, PHENIX: a comprehensive Python-based system for
466 macromolecular structure solution. *Acta Crystallographica Section D Biological*
467 *Crystallography* **66**, 213–221 (2010).
- 468 14. P. Emsley, K. Cowtan, Coot: model-building tools for molecular graphics.
469 *Acta Crystallographica Section D Biological Crystallography* **60**, 2126–2132
470 (2004).
- 471 15. S. Piana, P. Robustelli, D. Tan, S. Chen, D. E. Shaw, Development of a
472 Force Field for the Simulation of Single-Chain Proteins and Protein–Protein
473 Complexes. *J Chem Theory Comput* **16**, 2494–2507 (2020).
- 474 16. J. A. Maier, *et al.*, ff14SB: Improving the Accuracy of Protein Side Chain and
475 Backbone Parameters from ff99SB. *J Chem Theory Comput* **11**, 3696–3713.
- 476 17. D. Tan, S. Piana, R. M. Dirks, D. E. Shaw, RNA force field with accuracy
477 comparable to state-of-the-art protein force fields. *Proc National Acad Sci* **115**,
478 201713027 (2018).
- 479 18. S. Piana, A. G. Donchev, P. Robustelli, D. E. Shaw, Water Dispersion
480 Interactions Strongly Influence Simulated Structural Properties of Disordered
481 Protein States. *J Phys Chem B* **119**, 5113–5123 (2015).
- 482 19. K. J. Bowers, *et al.*, Scalable Algorithms for Molecular Dynamics Simulations
483 on Commodity Clusters. *Acm leee Sc 2006 Conf Sc'06*, 43–43 (2006).
- 484 20. D. E. Shaw, *et al.*, Anton 2: Raising the Bar for Performance and
485 Programmability in a Special-Purpose Molecular Dynamics Supercomputer. *Sc14*
486 *Int Conf High Perform Comput Netw Storage Analysis*, 41–53 (2014).
- 487 21. G. J. Martyna, D. J. Tobias, M. L. Klein, Constant pressure molecular
488 dynamics algorithms. *J Chem Phys* **101**, 4177–4189 (1994).
- 489 22. C. Predescu, *et al.*, Computationally efficient molecular dynamics integrators
490 with improved sampling accuracy. *Mol Phys* **110**, 967–983 (2012).

- 491 23. M. Tuckerman, B. J. Berne, G. J. Martyna, Reversible multiple time scale
492 molecular dynamics. *J Chem Phys* **97**, 1990–2001 (1992).
- 493 24. C. Predescu, *et al.*, The u -series: A separable decomposition for
494 electrostatics computation with improved accuracy. *J Chem Phys* **152**, 084113
495 (2020).
- 496 25. Y. Z. Tan, *et al.*, Addressing preferred specimen orientation in single-particle
497 cryo-EM through tilting. *Nature methods* **14**, 793–796 (2017).
- 498 26. V. B. Chen, *et al.*, MolProbity: all-atom structure validation for
499 macromolecular crystallography. *Acta Crystallographica Section D Biological
500 Crystallography* **66**, 12–21 (2010).
- 501 27. A. J. W. te Velthuis, Common and unique features of viral RNA-dependent
502 polymerases. *Cell Mol Life Sci Cmls* **71**, 4403–20 (2014).
- 503 28. T. D. Schneider, R. M. Stephens, Sequence logos: a new way to display
504 consensus sequences. *Nucleic Acids Research* **18**, 6097–6100 (1990).
- 505 29. M. Abdelkareem, *et al.*, Structural Basis of Transcription: RNA Polymerase
506 Backtracking and Its Reactivation. *Mol Cell* **75**, 298-309.e4 (2019).
- 507 30. D. Wang, *et al.*, Structural basis of transcription: backtracked RNA
508 polymerase II at 3.4 angstrom resolution. *Science* **324**, 1203–1206 (2009).
- 509 31. E. Jurrus, *et al.*, Improvements to the APBS biomolecular solvation software
510 suite. *Protein Sci* **27**, 112–128 (2018).
- 511 32. C. A. Schneider, W. S. Rasband, K. W. Eliceiri, NIH Image to ImageJ: 25
512 years of image analysis. *Nature methods* **9**, 671–675 (2012).

513